Solar Energy 159 (2018) 270–282

Contents lists available at ScienceDirect

Solar Energy

journal homepage: www.elsevier.com/locate/solener

Development and prototype testing of $MgCl_2$/graphite foam latent heat thermal energy storage system

Dileep Singh[a,*], Wenhua Yu[a], Weihuan Zhao[a,1], Taeil Kim[a], David M. France[a,b], Roger K. Smith[a]

[a] Energy Systems Division, Argonne National Laboratory, 9700 S. Cass Avenue, Argonne, IL 60439, USA
[b] Department of Mechanical and Industrial Engineering, University of Illinois at Chicago, 842 West Taylor Street (m/c 251), Chicago, IL 60607, USA

ARTICLE INFO

Keywords:
Magnesium chloride/graphite foam composite
Latent heat thermal energy storage
Prototype testing
Thermal simulations

ABSTRACT

Composites of graphite foam infiltrated with a magnesium chloride phase-change material have been developed as high-temperature thermal energy storage media for concentrated solar power applications. This storage medium provides a high thermal energy storage density, a narrow operating temperature range, and excellent heat transfer characteristics. In this study, experimental investigations were conducted on laboratory-scale prototypes with magnesium chloride/graphite foam composite as the latent heat thermal energy storage system. Prototypes were designed and built to monitor the melt front movement during the charging/discharging tests. A test loop was built to ensure the charging/discharging of the prototypes at temperatures > 700 °C. Repeated thermal cycling experiments were carried out on the fabricated prototypes, and the experimental temperature profiles were compared to the predicted results from numerical simulations using COMSOL Multiphysics software. Experimental results were found to be in good agreement with the simulations to validate the thermal models.

1. Introduction

Thermal energy storage (TES) systems have been developed for applications in concentrated solar power (CSP) electric plants to provide load leveling for grid electricity supply, to improve the overall plant efficiency, and to reduce the levelized cost of electricity (LCOE). TES systems allow electricity generation during nighttime and cloudy days, which is expected to reduce LCOE and help make CSP a competitive option to conventional technologies for electric power generation. Two general approaches can be applied to thermal energy storage systems, sensible heat storage and latent heat storage. Existing CSP plants that have a storage option use the sensible heat thermal energy storage systems (Burgaleta et al., 2011; Kuravi et al., 2013; Medrano et al., 2010). Recently, latent heat thermal energy storage (LHTES) systems have been attracting considerable interest because of their advantages over sensible heat thermal energy storage systems. LHTES systems have (a) a smaller storage system size resulting from the higher storage density based on the latent heat of fusion of a phase-change material (PCM) and (b) a narrower operation temperature range related to the melting/solidification temperature of the PCM which results in the potential of high exergy efficiencies (Jegadheeswaran et al., 2010).

For an LHTES system, in addition to the melting/solidification temperature and the latent heat of fusion of the PCM, the thermal conductivity of the PCM plays a key role on its thermal performance and, hence, its efficiency. Unfortunately, thermal conductivities of PCMs for LHTES systems applicable to CSP plants are usually very low (Zalba et al., 2003). Therefore, the heat transfer rate between the PCM and the charging/discharging heat transfer fluid (HTF) is quite low, and consequently a significantly large number of HTF tubes are required for charging or discharging an LHTES system within a reasonable time frame (e.g. 8–12 h for an LHTES system for a CSP plant). To improve the heat transfer rate, focus has been on improving the thermal performances of both PCM and the HTFs. In this regard, some of the approaches have been: finned HTF tubes (Lacroix, 1993; Miliozzi et al., 2015; Velraj et al., 1997) and heat pipes (Robak et al., 2011; Shabgard et al., 2010) for reducing the thermal resistance between the PCM and the HTF, dispersed high-thermal conductivity particles (Siegel, 1977) and metal foam structures (Hong and Herling, 2006; Krishnan et al., 2005; Siahpush et al., 2008; Zhao and Wu, 2011) or graphite foam (GF) structures (Kim et al., 2014; Singh et al., 2016; Zhao et al., 2014) for increasing the heat conduction inside the PCM, or a combination of these techniques (Nithyanandam and Pitchumani, 2013).

Based on previous theoretical analyses and numerical simulations by the authors (Kim et al., 2014; Zhao and Wu, 2011; Zhao et al., 2014),

---

[*] Corresponding author.
E-mail address: dsingh@anl.gov (D. Singh).
[1] Now with Department of Mechanical and Energy Engineering, University of North Texas, Denton, TX 76207, USA.

https://doi.org/10.1016/j.solener.2017.10.084
Received 21 April 2017; Received in revised form 23 August 2017; Accepted 29 October 2017

Nomenclature

$B(T)$	liquid fraction
c_p	mass specific heat capacity (J/kg K)
$d\alpha/dT$	Gaussian function
k	thermal conductivity (W/m K)
L	latent heat of fusion (J/kg)
t	time (s)
T	temperature (K)
V	volume (m^3)

Greek symbols

ρ	density (kg/m^3)
ϕ	open porosity of the graphite foam (%)
φ	infiltration rate (%)
ω	mass percentage of the $MgCl_2$ in the infiltrated graphite foam (%)

Subscripts

air	air
charging	charging process
discharging	discharging process
eff	effective
furnace	furnace
GF	graphite foam
infiltrated GF	infiltrated graphite foam
l	liquid
max	maximum
melting/solidification	melting or solidification
PCM	phase-change material
s	solid
xy	x-y plane
z	z direction

Acronyms

CSP	concentrated solar power
GF	graphite foam
HTF	heat transfer fluid
LCOE	levelized cost of electricity
LHTES	latent heat thermal energy storage
PCM	phase-change material
TC	thermocouple
TES	thermal energy storage

an LHTES system, using high thermal conductivity GF infiltrated with $MgCl_2$ as the storage medium, can significantly improve the heat transfer performance between the PCM and the HTF. This LHTES medium reduces the number of HTF tubes required for the LHTES system and increases the round trip exergy efficiencies of the LHTES system when compared to a similar LHTES system without GF. In this study, the LHTES medium was investigated further with the objectives of (a) experimentally investigating charging and discharging behaviors of the LHTES system with multiple prototype testing; (b) comparing experimental data with numerical predictions to validate and, if necessary, refine simulation models for predicting the thermal characteristics of such LHTES systems; and (c) determining the effect of thermal cycling and PCM redistribution on thermal performance.

2. Experimental

2.1. Prototype design

The main components of each prototype included a PCM/GF composite, a container cylinder, a top plate, a bottom plate, an HTF tube, a vacuum port, thermocouples (TCs), and thermocouple connectors. As shown schematically in Fig. 1, the container cylinder was made of Incoloy 800H with an outside diameter of 4.5 in. and a wall thickness of 0.34 in.; the top and bottom plates were made of Incoloy 800H as well; the HTF tube was made of Incoloy 800H with an outside diameter of 0.5 in. and a wall thickness of 0.03 in.; and the vacuum port was made of Incoloy 800H tubing with an outside diameter of 0.125 in. and a wall thickness of 0.02 in. Incoloy 800H was used as the material for the main components of the prototypes because of its resistance to oxidation at high temperatures. The GF was brazed to the container cylinder, the bottom plate, and the HTF tube by using a commercial brazing alloy to eliminate any air gaps between the GF and the other components. The heights of the container cylinder and the PCM/GF composite were 6 in. and 5 in., respectively. In this study, $MgCl_2$ was used as the PCM. There was approximately 2.0 kg of the $MgCl_2$/GF storage medium in each prototype. However, the precise mass value of each prototype was used for both simulations and experimental data analysis.

2.2. Infiltration of $MgCl_2$

For each laboratory-scale prototype, a vacuum and pressure-assisted melting process was used to infiltrate $MgCl_2$ into the GF within the prototype container through the following steps. First, $MgCl_2$ powder and the container with the GF were placed in two chambers separated by a valve. Second, the $MgCl_2$ chamber was heated to > 800 °C under an argon environment, and the GF chamber was evacuated and heated up to 800 °C. Third, after the $MgCl_2$ powder completely melted, the valve separating the two chambers was opened to allow the melted $MgCl_2$ to infiltrate the GF with the system pressurized from the $MgCl_2$ chamber side to ensure complete infiltration of the GF with $MgCl_2$. After the infiltration process, any excess $MgCl_2$ was removed.

The infiltration rate or the amount of the $MgCl_2$ in each prototype is a key quantity for calculating the energy stored in, or released from, the $MgCl_2$/GF composite medium. This value was also important for comparing the experimental data from charging or discharging to the predicted results from numerical simulations and for evaluating the performance of the LHTES system based on experimental data. In this study, the accurate determination of the $MgCl_2$ amount was achieved through carefully measuring the mass of the prototype container/GF combination prior to and after the $MgCl_2$ infiltration process to determine the infiltration rates.

2.3. Experimental test facility

The experimental test facility (as shown in Fig. 2) used in this study was an open loop system consisting mainly of an air-flow pump, an air heater, a furnace, and a ventilation hood. It was designed and fabricated to study the charging and discharging characteristics of laboratory-scale prototypes of LHTES systems at temperatures up to 1000 °C. The air pump is controlled by a voltage regulator to provide a stable air-flow rate in the experimental test loop. The capacity of the air pump is in the range of 1.67×10^{-3}–$8.33 \times 10^{-3}\ m^3/s$. The air heater is equipped with temperature interlocks for protecting it from overheating. The laboratory-scale prototype was placed inside a furnace and was connected to the experimental test loop.

During a typical experiment, prototype was held at a fixed furnace temperature and the charging/discharging was conducted by the

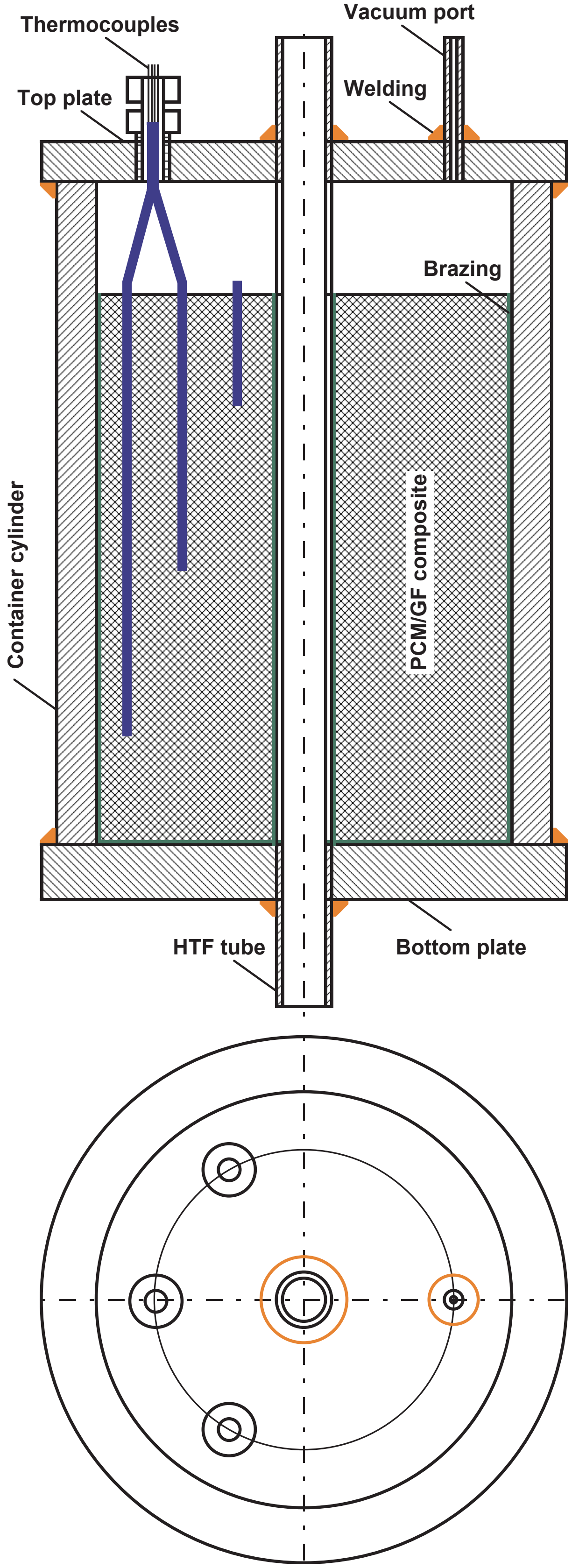

Fig. 1. Overall view of laboratory-scale LHTES prototype.

flowing air maintained at appropriate temperatures. The HTF (air) was pumped at a specific flow rate into the air heater in which it was heated from room temperature to a desired higher temperature for charging process or discharging process. The high-temperature air flowed through the HTF tube at the center of the prototype to melt or solidify the PCM for the charging process or the discharging process, respectively. The air then exited the prototype HTF tube into the ventilation hood. During experiments, the air-flow rate was monitored by a NIST-traceable flow meter, which was installed at the outlet of the air pump. Air temperatures were measured at several locations along the experimental test loop including the inlet and outlet of the air heater and the inlet and outlet of the prototype. A data acquisition system was used to record the following experimental parameters for further data reduction: air flow rate, air pressure, air temperatures, and PCM temperatures at various locations inside the prototype as discussed in detail below.

Fig. 2. Photograph of the experimental test facility for prototype testing.

2.4. Test prototypes

In this study, charging and discharging experimental tests were conducted on three laboratory-scale prototypes: Prototype 1, Prototype 2, and Prototype 3. Two types of GFs were used for these prototypes. For Prototype 1 and Prototype 3, Kfoam® with an open porosity of approximately 84% from Koppers, Inc., was used; and for Prototype 2, Graftech foam with an open porosity of approximately 90% from GrafTech International was used. Thermocouples were inserted into the $MgCl_2$/GF composite through holes pre-drilled in the $MgCl_2$/GF composite to measure temperatures at various locations (radii and depths). The details of thermocouple distributions are shown schematically in Fig. 3. High-temperature type S thermocouples were used in these prototypes because of their chemical resistance to the PCM ($MgCl_2$). To determine their measurement accuracies and offsets at elevated temperatures, the thermocouples were carefully calibrated against a standard NIST-traceable type K thermocouple at temperatures around 760–770 °C before they were installed into the prototypes. The calibration corrections were incorporated in experimental data reduction and subsequent analyses.

2.5. Experimental test procedure

The experimental testing of a prototype involved four major steps: prototype placement into the experimental test loop, moisture removal from the prototype, prototype charging testing, and prototype discharging testing.As shown schematically in Fig. 4, the prototype was connected to the experimental test loop, through the Swagelok® connectors at both ends of the HTF tube of the test prototype, at the inlet port from the heater and the air pump and at the outlet port to the vent. The vacuum port was connected to the vacuum pump and a compressed argon cylinder for removing moisture and for controlling $MgCl_2$/GF composite environment. Thermocouple wires were connected to the data acquisition system. In addition, the prototype was thermally

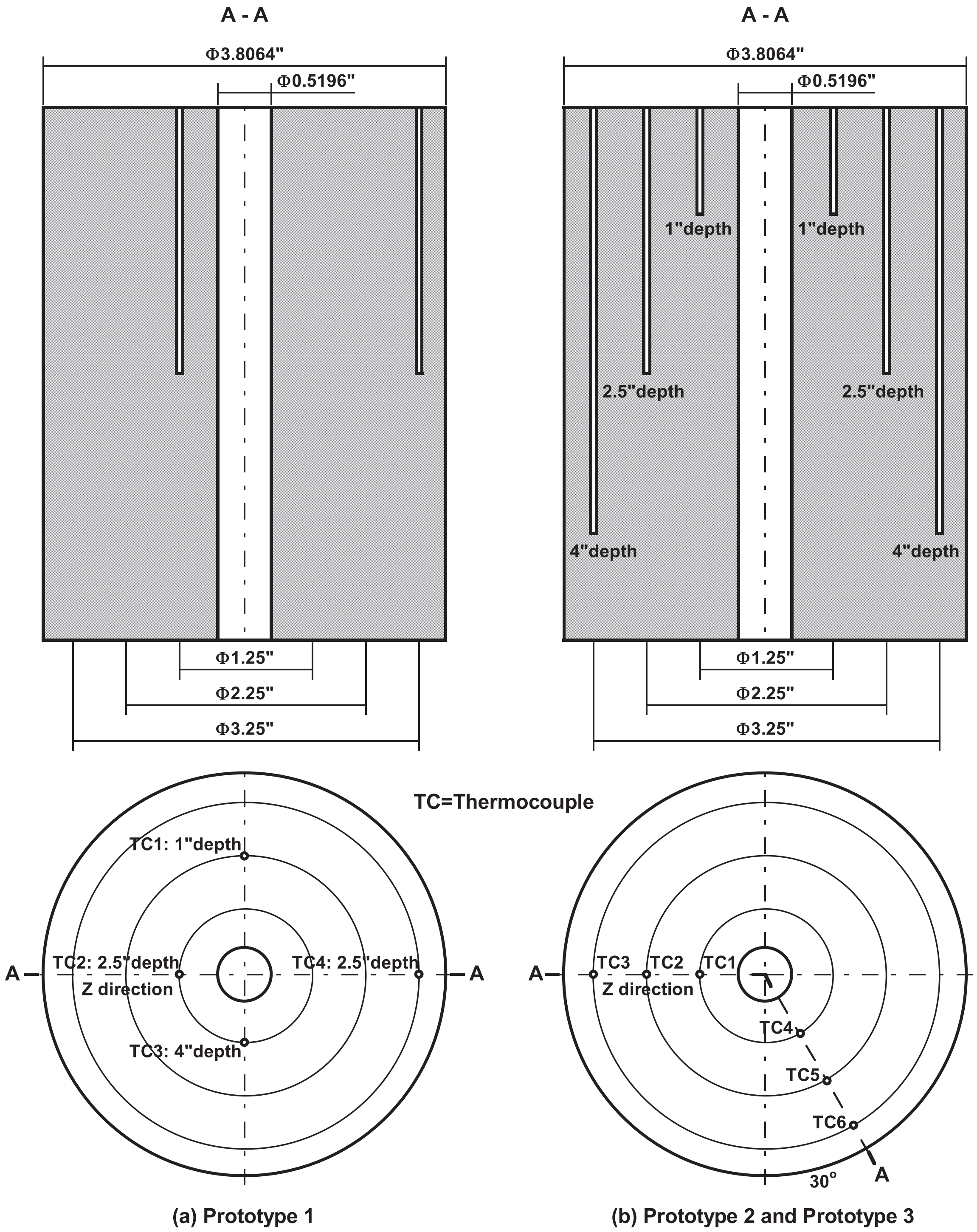

Fig. 3. Distribution of thermocouples in the $MgCl_2$/GF composite.

insulated with a 2-in. high-temperature ceramic fiber blanket wrapped around its container. The HTF tube, extending outside the prototype, was also insulated to minimize heat loss or gain from the tube during charging or discharging process. Two thermocouples were installed at the outside surface of the prototype cylinder and the outside surface of insulation for calibrating prototype heat loss to the furnace during charging and prototype heat gain from the furnace during discharging.

Prior to charging/discharging experiments for each prototype, any moisture absorbed in $MgCl_2$ PCM was removed by heating and evacuation. First, the prototype was evacuated down to approximately 2 psi at room temperature by using the vacuum pump. The pressure was monitored during a 24-h period to ensure vacuum-tight sealing of all prototype components and connections. Second, the prototype was heated to 400 °C and held at that temperature for 24 h. During this time period, the prototype was evacuated as frequently as necessary, especially for the prototype temperature above 250 °C to maintain the pressure 2–5 psi. Third, the prototype was heated to 600 °C and held at that temperature for 24 h. The prototype pressure increased again when its temperature was above 500 °C. The prototype was again evacuated as frequently as necessary until there was no appreciable increase in pressure. Finally, the prototype was cooled down to room temperature. After the moisture removal process, prototype was back filled with

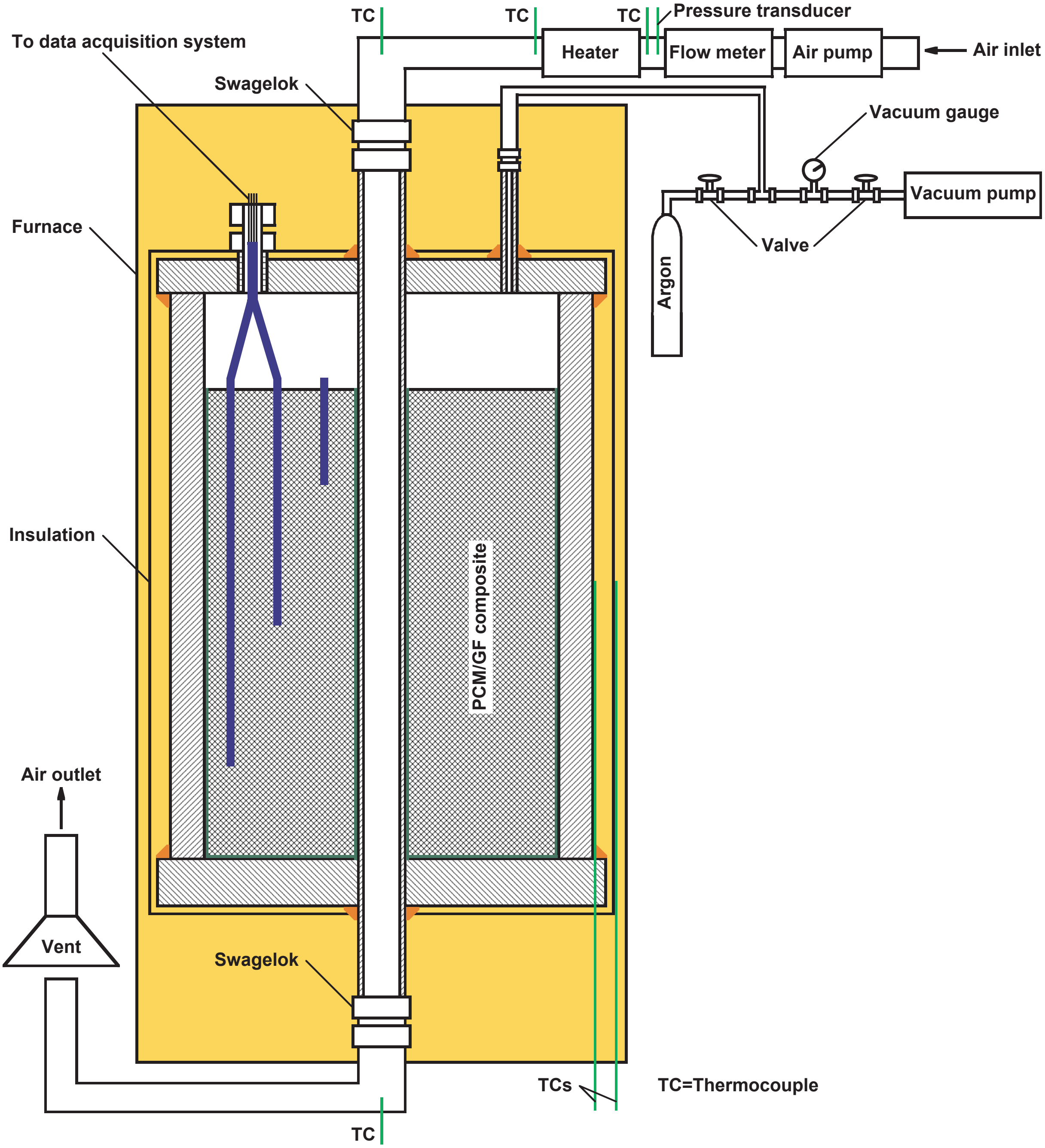

Fig. 4. Prototype connection in the experimental test loop *(not to scale)*.

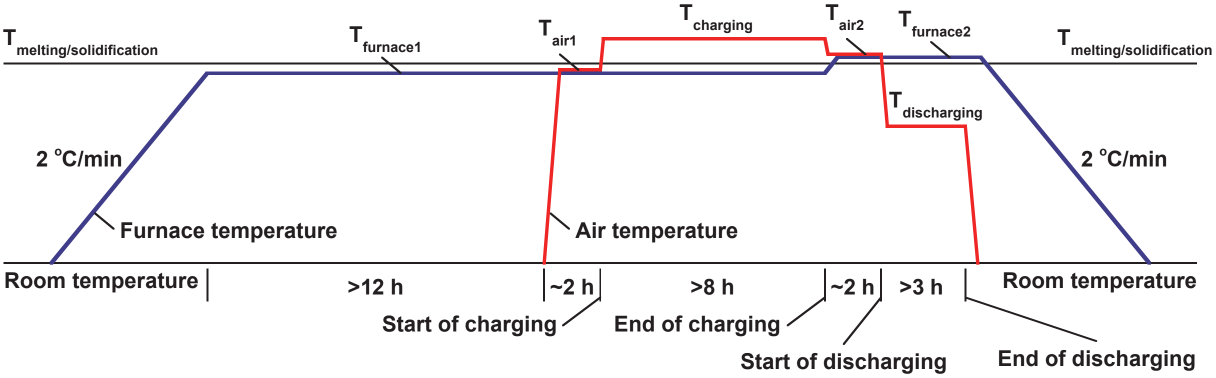

Fig. 5. Furnace and heater temperature settings for charging/discharging tests.

argon gas to create an argon environment within the prototype.

As shown in Fig. 5, charging and discharging were generally conducted in one test cycle. First, the furnace was preheated to a temperature $T_{furnace1}$ (lower than the $MgCl_2$ melting/solidification temperature $T_{melting/solidification}$) and was kept at that temperature long enough to allow a temperature equilibrium of the prototype inside the furnace. Second, the air pump was started and air was heated to an air inlet temperature T_{air1} (lower than $T_{melting/solidification}$) of the prototype. The test system was kept at that condition for approximately 2 h for the prototype to reach an equilibrium state. Third, the charging process was started by increasing the heater controller setting to achieve an air inlet temperature $T_{charging}$ of the prototype. Fourth, after the charging process, the furnace temperature was increased to $T_{furnace2}$ (higher than $T_{melting/solidification}$), and the heater temperature was reduced to an air inlet temperature T_{air2} (higher than $T_{melting/solidification}$) of the prototype. The test system was kept at that condition for approximately 2 h for the prototype to reach an equilibrium state. Fifth, the discharging process was started by decreasing the heater controller setting to give an air inlet temperature $T_{discharging}$ of the prototype. Finally, after the discharging process, the prototype was cooled down to room temperature.

3. Numerical simulations

Numerical simulations using COMSOL Multiphysics commercial software were conducted for the prototypes to investigate the heat transfer performance of the $MgCl_2$/GF composite. Simulation results were compared with the experimental measurements data to validate the simulation model as well as the thermal properties of the $MgCl_2$/GF composite used in the simulations.

3.1. Modeling geometry

Three-dimensional modeling was used in this study to include the anisotropic nature of the graphite foam thermal conductivity. The three-dimensional computational model simulating the prototype geometry (shown in Fig. 6) was based on the experimental test system described above. The HTF (air) was flowing in the center tube to transport thermal energy to the storage medium, prototype container, and insulation material outside the container. The boundary condition outside the insulation was considered as the combined convection and radiation heat transfer to the furnace environment. For the thermal energy storage medium $MgCl_2$/GF composite, the $MgCl_2$ was infiltrated into the GF for each prototype and its infiltration rate φ (the ratio of the infiltrated $MgCl_2$ volume to the total porosity volume) was calculated based on the following equation (Singh et al., 2016):

$$\varphi = \frac{V_{PCM}}{\phi_{GF} V_{GF}} \tag{1}$$

where V is the volume and ϕ is the open porosity. According to the weight measurements of each prototype before and after the infiltration process, the total mass of the $MgCl_2$ infiltrated into the GF was obtained for each prototype, and the infiltration rate was calculated based on the above equation. Based on the infiltration rate, the thermal properties of the infiltrated GF were calculated. Table 1 summarizes the properties of each prototype in the simulations.

The thermal conductivities of the infiltrated GFs in Table 1 were measured by the Xenon-Flash Diffusivity Analyzer (Singh et al., 2016). The latent heat of fusion, specific heat, and density of the infiltrated GFs in Table 1 were calculated based on the infiltration rate for each prototype by the following equations, respectively (Singh et al., 2015):

$$L_{infiltrated\ GF} = L_{PCM}\,\omega \tag{2}$$

$$c_{p\,infiltrated\ GF} = c_{p\,PCM}\,\omega + c_{p\,GF}(1-\omega) \tag{3}$$

$$\rho_{infiltrated\ GF} = \rho_{PCM}\,\varphi\phi_{GF} + \rho_{GF}(1-\phi_{GF}) \tag{4}$$

where L is the latent heat of fusion, c_p is the specific heat, ρ is the density, ω is the mass percentage of the $MgCl_2$ in the infiltrated GF. Thermophysical properties of the $MgCl_2$ and the GF are based on the literature values from the authors and other researchers (Singh et al., 2016, 2015; Poling et al., 2008; Janz et al., 1979). The thermal properties illustrated in Table 1 were used in the numerical simulations.

3.2. Heat transfer simulations

Because of the small pore size and the high thermal conductivity of the GF, the heat was expected to exchange very fast between the $MgCl_2$ and the GF, leading to the $MgCl_2$ and the GF in a local thermal equilibrium (Wu and Xing, 2010). The $MgCl_2$ and graphite can be considered to have the same temperature at the interface (Guo et al., 2015; Ohsenbrügge et al., 2016; Wu and Xing, 2010). Therefore, the equilibrium thermal model was applied to simulate the heat transfer process of the $MgCl_2$/GF composite as follows:

$$\rho_{infiltrated\ GF}\, c_{peff} \frac{\partial T}{\partial t} = \nabla\cdot(k\nabla T) \tag{5}$$

In the above equation, T is the temperature, t is the time, and k is the thermal conductivity of the $MgCl_2$/GF composite.

The equivalent heat capacity method was applied to the phase-change simulations (Faghri et al., 2010; Zhao et al., 2014). The specific heat c_{peff} of the storage medium (the $MgCl_2$/GF composite) is represented in the following equation (Samara et al., 2012; Singh et al., 2015; Zhao et al., 2014):

$$c_{peff} = c_{p\,infiltrated\ GF,s} + (c_{p\,infiltrated\ GF,l} - c_{p\,infiltrated\ GF,s})B(T) + L_{infiltrated\ GF}\frac{d\alpha}{dT} \tag{6}$$

where $B(T)$ is the liquid fraction (Samara et al., 2012; Singh et al., 2015; Zhao et al., 2014), da/dT is the Gaussian function (Samara et al., 2012; Singh et al., 2015; Zhao et al., 2014), and the subscripts l and s indicate the liquid-state storage medium and the solid-state storage medium, respectively. The above equation enables integrating the latent heat of fusion into the heat capacity for the phase-change process simulations.

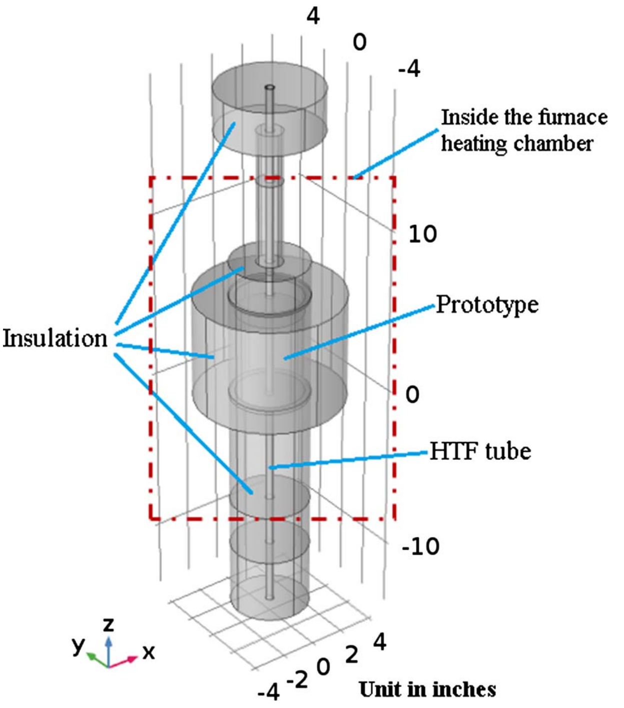

Fig. 6. Modeling geometry of the prototype system in numerical simulations.

Table 1
Properties of the $MgCl_2$/GF composite (Singh et al., 2016; Singh et al., 2015; Janz et al., 1979).

	Prototype 1	Prototype 2	Prototype 3
GF open porosity (volume %)	84	90	84
Infiltrated rate of liquid $MgCl_2$ (φ_l)	1.19	1.20	1.26
Infiltrated rate of solid $MgCl_2$ (φ_s)	0.86	0.87	0.91
Mass percentage of $MgCl_2$ for the infiltrated GF (%)	82.4	88.9	83.1
$MgCl_2$ melting point (°C) (DSC measurement)	718	718	718
$MgCl_2$ solidification point (°C) (DSC measurement)	706	706	706
Melting/solidification range[a] (°C)	8	8	8
Latent heat of fusion (kJ/kg)	373.9 (Singh et al., 2015)	403.6 (Singh et al., 2015)	377.3 (Singh et al., 2015)
Density (kg/m^3)	2050 (Singh et al., 2015; Janz et al., 1979)	2035 (Singh et al., 2015; Janz et al., 1979)	2137 (Singh et al., 2015; Janz et al., 1979)
Specific heat (J/kg K) (at 700 °C)	1074 (Singh et al., 2015; Janz et al., 1979)	1018 (Singh et al., 2015; Janz et al., 1979)	1068 (Singh et al., 2015; Janz et al., 1979)
Thermal conductivity (W/mK) (k_{xy} at 700 °C)	14.0 (Singh et al., 2016)	9.3 (Singh et al., 2016)	14.0 (Singh et al., 2016)
Thermal conductivity (W/mK) (k_z at 700 °C)	23.6 (Singh et al., 2016)	21.4 (Singh et al., 2016)	23.6 (Singh et al., 2016)

[a] The temperature range between the start and the end of melting/solidification for the prototype.

The initial temperatures in the simulations before each charging/discharging process were based on the thermocouple temperature recordings in the prototypes. The initial temperatures of the prototypes were approximately 690 °C for the charging process and 750 °C for the discharging process. The room-temperature air-flow velocities in the HTF tube were 2.92×10^{-3}–3.08×10^{-3} m^3/s and 3.17×10^{-3}–3.33×10^{-3} m^3/s for the charging process and the discharging process, respectively. The slightly higher air-flow velocity during the discharging process was due to the decrease of the air viscosity at lower temperatures. The actual furnace temperatures were kept at 700 °C for the charging process (lower than the melting point of $MgCl_2$) and 750 °C for the discharging process (higher than the solidification point of $MgCl_2$) to ensure that the melting/solidification process was driven by the HTF air from the center tube in the prototype only. The heat loss/heat gain from the prototype during the thermal cycling was calculated according to the actual furnace temperature (recorded by the thermocouple placed at the outer surface of the prototype insulation material in the furnace) and the convection and radiation heat transfer coefficients in the furnace around the prototype. Because the air in the furnace is almost stationary with very low natural convection, the major heat loss/heat grain to/from the furnace was caused by radiative heat transfer.

Fig. 7 shows the mesh structure for the $MgCl_2$/GF prototype system in the simulations. Fig. 7a is the mesh structure for the outside insulation material and Fig. 7b is the finer mesh structure for the inside prototype. The model consists of 385,981 domain elements, 32,842 boundary elements, and 4127 edge elements. Based on a mesh independence study, these mesh elements are sufficient in the three-dimensional numerical simulations for the prototype heat transfer processes.

4. Results and Discussions

4.1. Experimental test conditions

Charging and discharging tests were conducted for Prototype 1, Prototype 2, and Prototype 3. For each prototype, the charging process and the discharging process were carried out in one test cycle and repeat test cycles were performed. The detailed furnace and heater temperature settings for charging/discharging tests are listed in Table 2. During each charging process or discharging process, the air-flow rate was not adjusted; however, small fluctuations existed due to air temperature changes. All readings from various sensors including the thermocouples, the air flow meter, and the air pressure transducer were automatically logged into the data acquisition computer in a predetermined time interval of 6 s.

There were some issues with the thermocouple readings of the prototypes during charging/discharging tests. The high temperatures and the GF caused problems with grounding and/or shorting. The results reported below are from the thermocouples with showed stable readings during the entire charging/discharging tests.

4.2. Typical temperature curves

For illustrative purposes, typical temperatures (by TC4 of Prototype 3 in Test 4) in the prototype measured as functions of the time for the charging and the discharging processes are shown in Fig. 8a and b, respectively. For the charging process, the $MgCl_2$ changed from the solid state to the liquid state through three thermal energy storage stages. First, the solid $MgCl_2$/GF was heated and its temperature increased as a result of sensible heat energy storage. Second, when the $MgCl_2$ temperature was high enough, the solid $MgCl_2$ started melting and latent heat energy storage occurred. Third, when the melting process completed, the liquid $MgCl_2$ and GF was heated and its temperature increased again as a result of sensible heat energy storage. For the

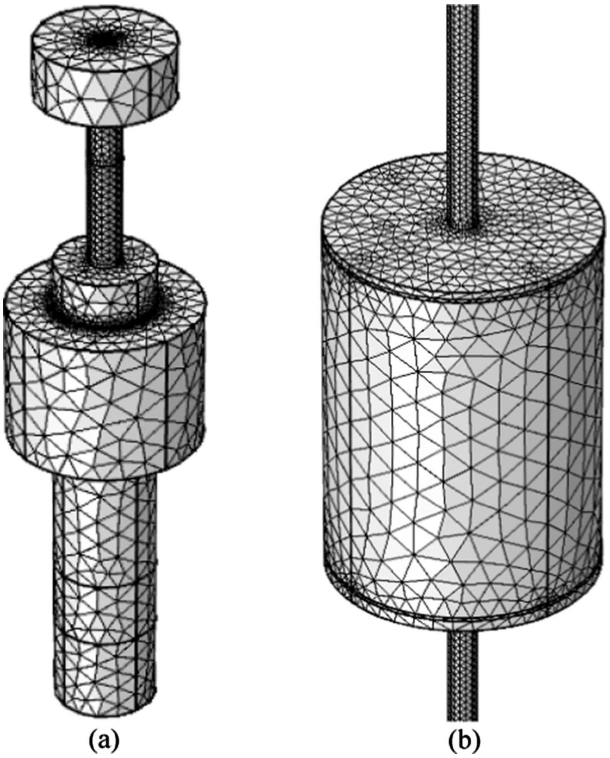

Fig. 7. Mesh structure in numerical simulations.

Table 2
Temperature settings for charging/discharging tests.

Test	Temperature	Prototype 1	Prototype 2	Prototype 3
Test 1	$T_{furnace1}$	695 °C	685 °C	680 °C
	T_{air1}	715 °C	710 °C	710 °C
	$T_{charging}$	800 °C	800 °C	800 °C
	$T_{furnace2}$	735 °C	735 °C	735 °C
	T_{air2}	750 °C	750 °C	750 °C
	$T_{discharging}$	500 °C	500 °C	500 °C
Test 2	$T_{furnace1}$	695 °C	685 °C	680 °C
	T_{air1}	715 °C	710 °C	710 °C
	$T_{charging}$	800 °C	800 °C	800 °C
	$T_{furnace2}$	735 °C	735 °C	735 °C
	T_{air2}	750 °C	750 °C	750 °C
	$T_{discharging}$	500 °C	500 °C	500 °C
Test 3	$T_{furnace1}$	685 °C	685 °C	680 °C
	T_{air1}	715 °C	710 °C	710 °C
	$T_{charging}$	800 °C	800 °C	800 °C
	$T_{furnace2}$	735 °C		735 °C
	T_{air2}	750 °C		750 °C
	$T_{discharging}$	500 °C		500 °C

discharging process, the $MgCl_2$ changed from the liquid state to the solid state through three thermal energy release stages. First, the liquid $MgCl_2$/GF was cooled and its temperature decreased as a result of sensible heat energy release. Second, when the $MgCl_2$ temperature was low enough, the liquid $MgCl_2$ started solidification and latent heat energy release occurred. Third, when the solidification process completed, the solid $MgCl_2$/GF was cooled and its temperature decreased again as a result of sensible heat energy release. It can be seen from Fig. 8 that both melting and solidification processes happened in a quite narrow temperature range. All of these stages reflect typical behaviors of PCMs.

4.3. Temperature repeatability

It was expected that a redistribution of $MgCl_2$ in the $MgCl_2$/GF composite would occur after an initial charging/discharging process. This redistribution might affect the thermal performance of the LHTES system. To quantitatively assess this effect, multiple charging/discharging cycles were carried out for each test prototype and temperatures mesured by the same thermocouple were compared for those charging/discharging cycles. As an example, Fig. 9 shows temperatures measured for all charging/discharging cycles by TC1 in Prototype 1, Prototype 2, and Prototype 3, respectively. It can be seen from Fig. 9 that, while there are some differences in the temperature measurements, all charging temperature curves and discharging temperature curves follow very similar trends. Moreover, the temperature measurement differences are generally small. Comparisons for temperatures measured by other thermocouples are similar (within 2%) for the three prototypes tested. For relative comparison, also shown in Fig. 9 are the temperature profiles ± 3% from the average results of all the tests. It should be pointed out that test conditions such as the air flow rate and the initial prototype temperature for each charging/discharging cycle were close, but not exactly the same. It can be concluded from these results that (a) the $MgCl_2$ redistribution is minimal and its effect on heat transfer of the LHTES system is insignificant and (b) the thermal performance of the LHTES system is repeatable with regard to charging/discharging cycles.

As mentioned previously, for the purpose of investigating the GF type effect on the thermal performance of the LHTES system, the GF used in Prototype 2 was different from those used in Prototypes 1 and 3. Fig. 10 shows a comparison of temperatures as averages of measurements by TC1 in Prototypes 2 and 3 for all charging/discharging cycles. It can be seen from Fig. 10 that, despite some different test conditions such as the furnace temperature settings for the charging process (685 °C for Prototype 2 and 680 °C for Prototype 3), the average temperatures for both the charging process and the discharging process are quite similar for Prototypes 2 and 3. Therefore, the GF type is not critical as long as it has a high enough thermal conductivity for effectively conducting heat from the HTF to the $MgCl_2$/GF composite during the charging process and from the $MgCl_2$/GF composite to the HTF during the discharging process.

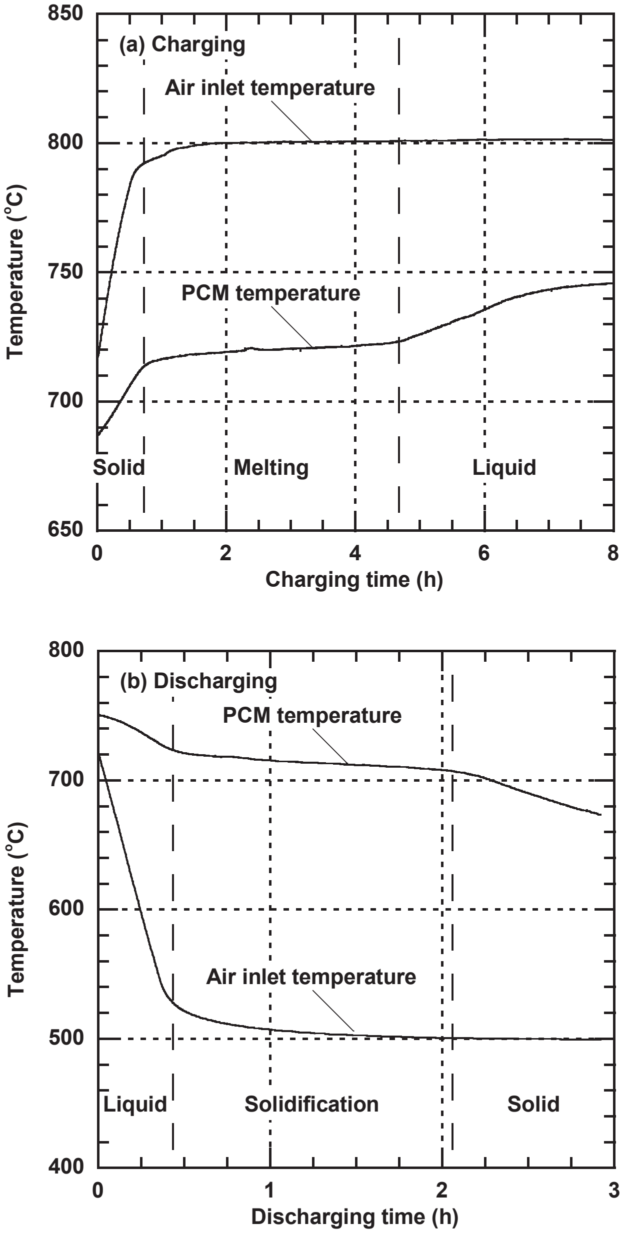

Fig. 8. Typical charging and discharging temperatures as functions of the time.

4.4. Comparison of experimental data and simulation results

For each charging/discharging test of all prototypes, numerical simulations were conducted according to the test conditions, and a comparison between the experimental data and the simulation results was performed. Figs. 11–13 display the comparison of the temperature profiles in Prototype 1, Prototype 2, and Prototype 3 between the experimental data and the simulation results during the first charging/discharging thermal cycle, respectively. Due to the high thermal conductivity of $MgCl_2$/GF composite, the heat transport was fast inside the prototype. Therefore, the temperature profiles did not show significant difference at various locations in the prototypes (as shown in

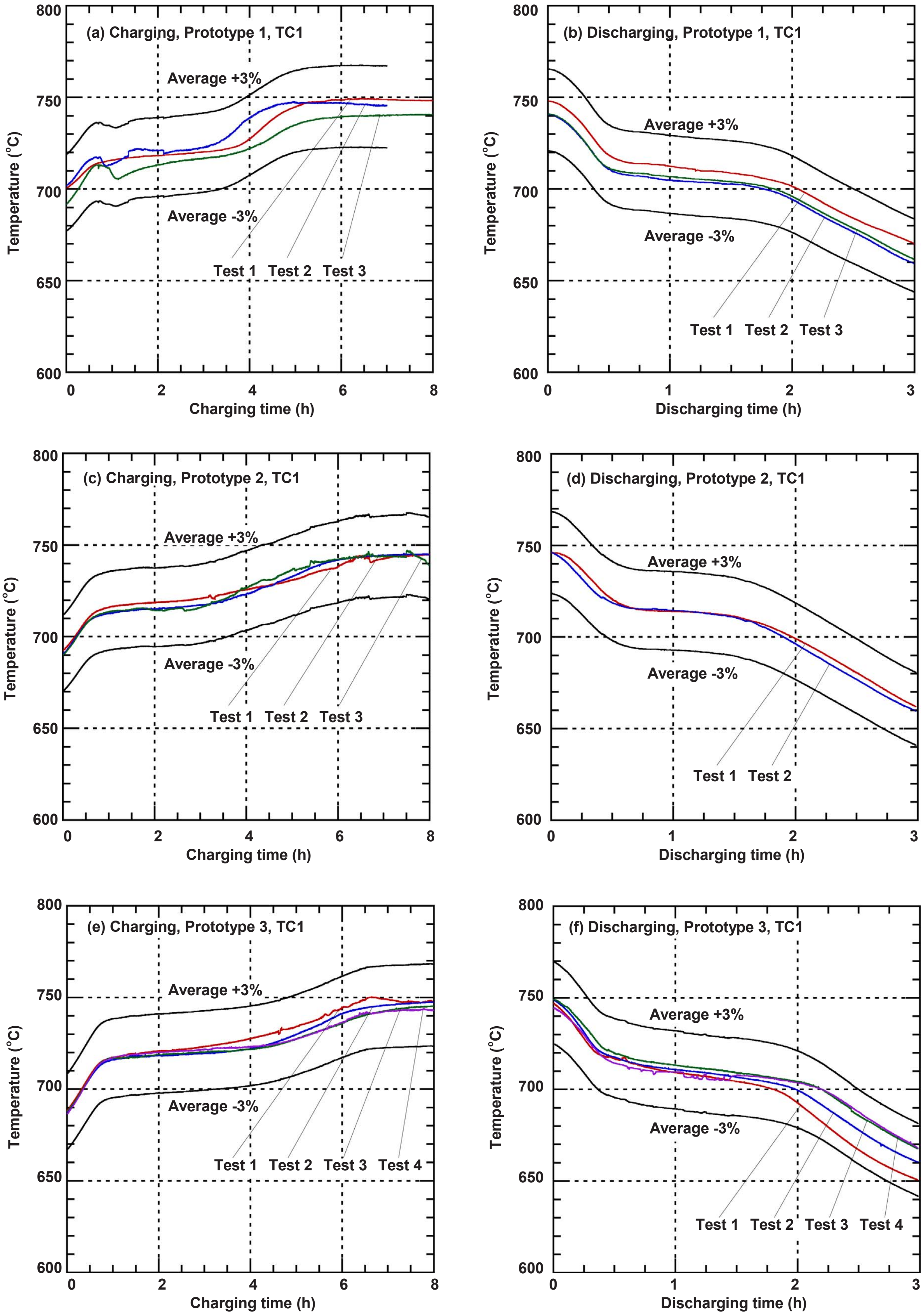

Fig. 9. Temperature repeatability of charging and discharging cycles.

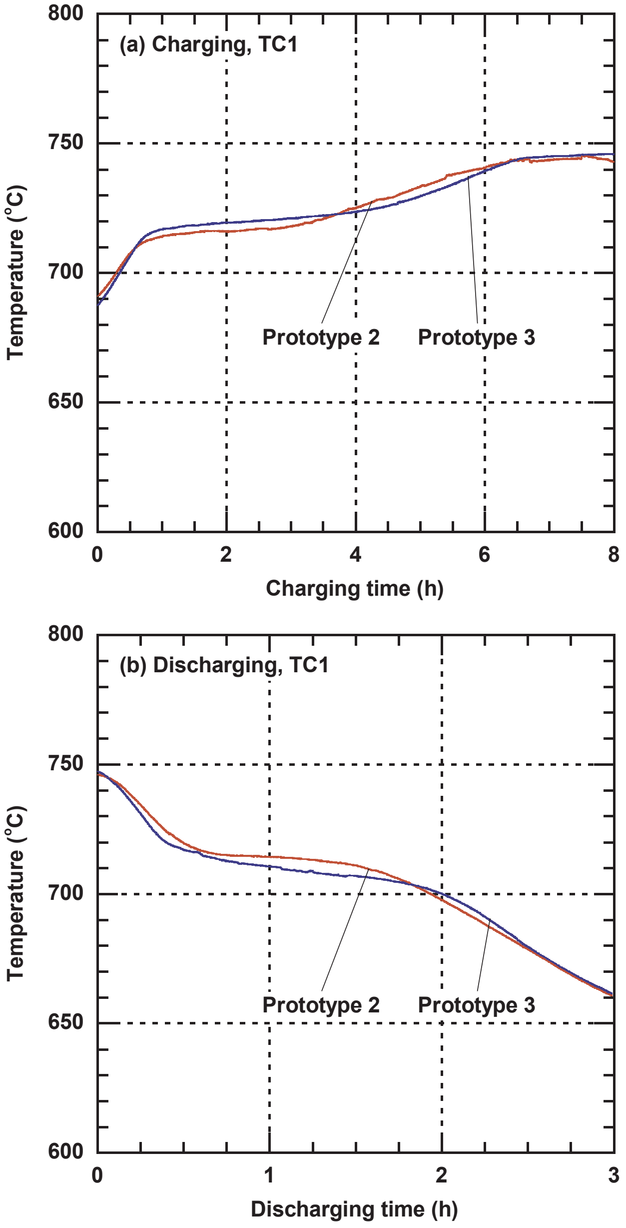

Fig. 10. Temperature comparisons of Prototypes 2 and 3 during charging and discharging.

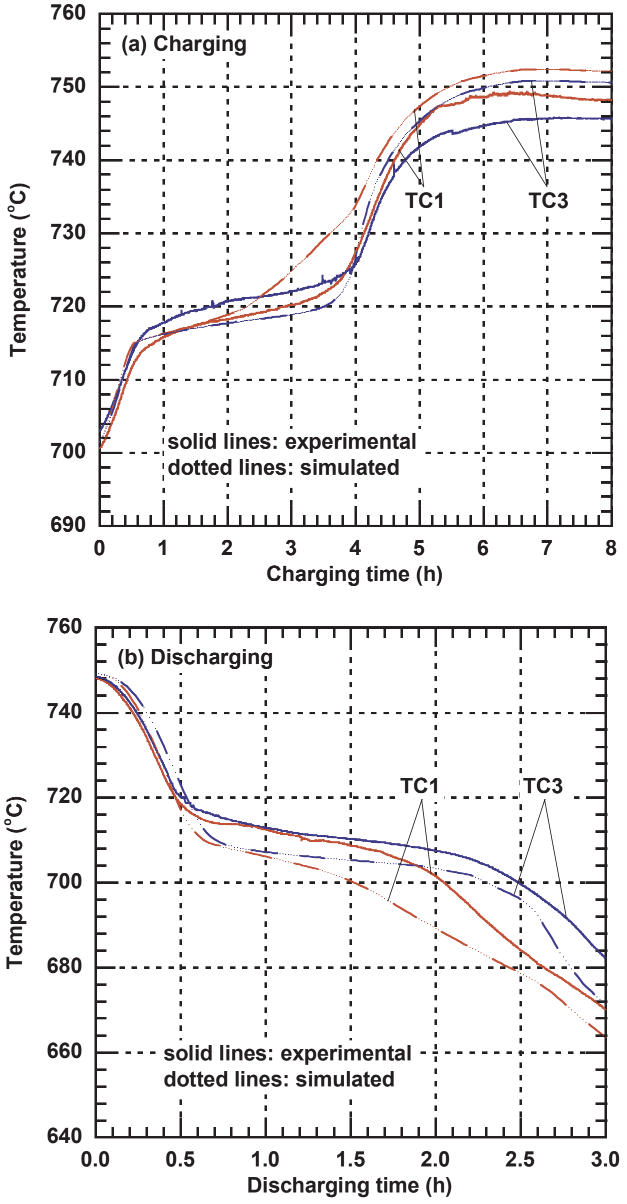

Fig. 11. Temperature comparison of experimental data and simulation results for Prototype 1 during (a) charging and (b) discharging.

Figs. 11–13). Three of the four thermocouples inserted in Prototype 1, as shown in Fig. 3, functioned properly during cycle testing. The temperatures at the corresponding thermocouple locations of TC1 and TC3 obtained from the numerical simulations were exported for comparing with the measurement data. As shown in Fig. 11, the simulation results match with the experimental data quite well. The total charging time for Prototype 1 was approximately 7 h (from the initial temperature of 700 °C to 750 °C) while the total discharging time was approximately 3 h (from 750 °C to 670 °C). Very similar results were obtained for other tests and other prototypes, shown in Figs. 12 and 13 for Prototype 2 and Prototype 3, respectively. For Prototype 2 shown in Fig. 12, the simulations showed different temperature trends for the two thermocouple locations (TC1 and TC6), while the experiments showed very similar temperature trends for them. The exact reason is not clear at this point. However, this observation did not occur for Prototypes 1 and 3. The quantitative time comparisons between the experimental data and the simulation results for Prototype 1, Prototype 2, and Prototype 3 are listed in Tables 3–8. The positive/negative number implies that the simulation result is faster/slower than the experimental observation.

Tables 3 and 4 illustrate the detailed difference between the measurement data and the simulation results for Prototype 1 during multiple charging and discharging processes, repectively. Based on the comparison between the experimental data and the numerical simulation results for three thermocouple locations of TC1, TC2, and TC3 in Prototype 1, the temperature measurement data match the simulation results well for multiple thermal cycles with a difference less than 2%. For the three charging process tests, the time differences at 730 °C (the temperature at which the melting process completes) between the experiments and the simulations are within 10% for all three thermocouple locations, as illustrated in Table 3. For the three discharging process tests, most of the time differences at 700 °C (the temperature at which the solidification process completes) between the experiments and the simulations are within 15% for the three thermocouple locations, as illustrated in Table 4.

Prototype 2 with a different type of GF from Prototype 1 was tested under the same conditions to further verify the simulation model and thermal properties of the $MgCl_2$/GF composite. Tables 5 and 6 illustrate

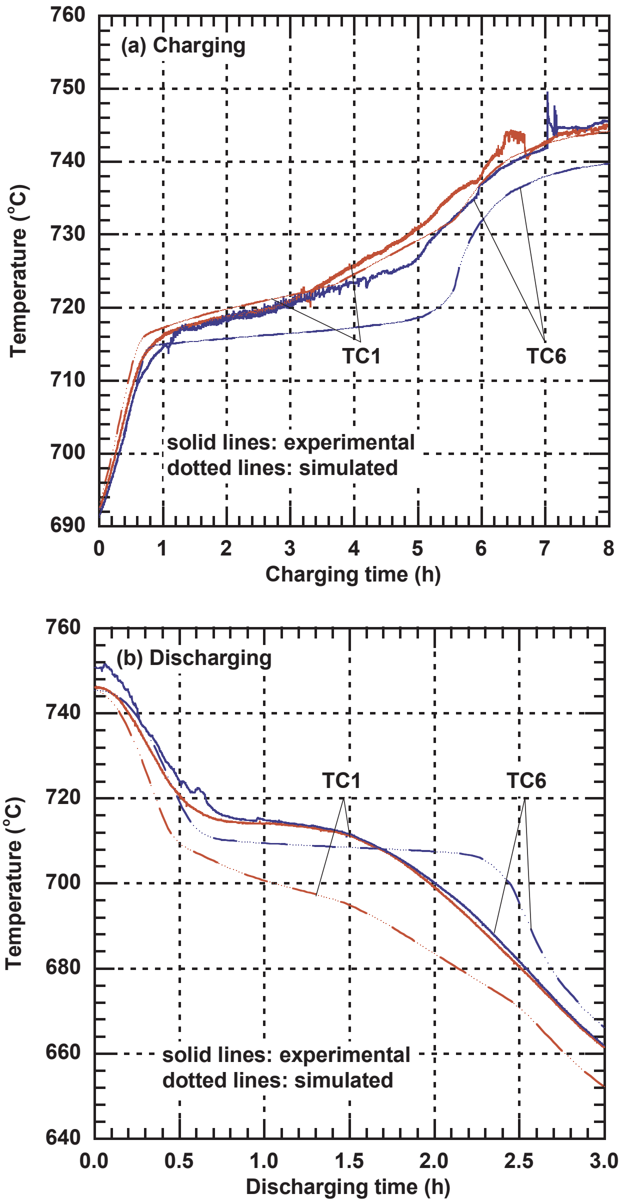

Fig. 12. Temperature comparison of experimental data and simulation results for Prototype 2 during (a) charging and (b) discharging.

the difference between the measurement data and the simulation results for Prototype 2 during the charging and discharging processes, respectively. The comparisons are for the thermocouple locations of TC1, TC2, TC5, and TC6 shown in Fig. 3. The temperature measurements from these thermocouples match the simulation results very well for both charging and discharging processes with the differences less than 2.5%. For the charging process, the time differences between the measurements and the simulations to reach 730 °C are within 15%. For the discharging process, most of the time differences to reach a specific temperature are also within 15% for Prototype 2, as illustrated in Tables 5 and 6. Only two points for TC1 have the time differences beyond the 15% during the discharging process. It is because the total charging time was approximately 8 h while the total discharging time was shorter, only around 3 h. Therefore, the percentage of time differences at a certain temperature was bigger for the discharging process than for the charging process. However, the absolute values of the time differences between the experimental data and the simulation results from the discharging processes were similar as those from the charging processes, as shown in Tables 3–8.

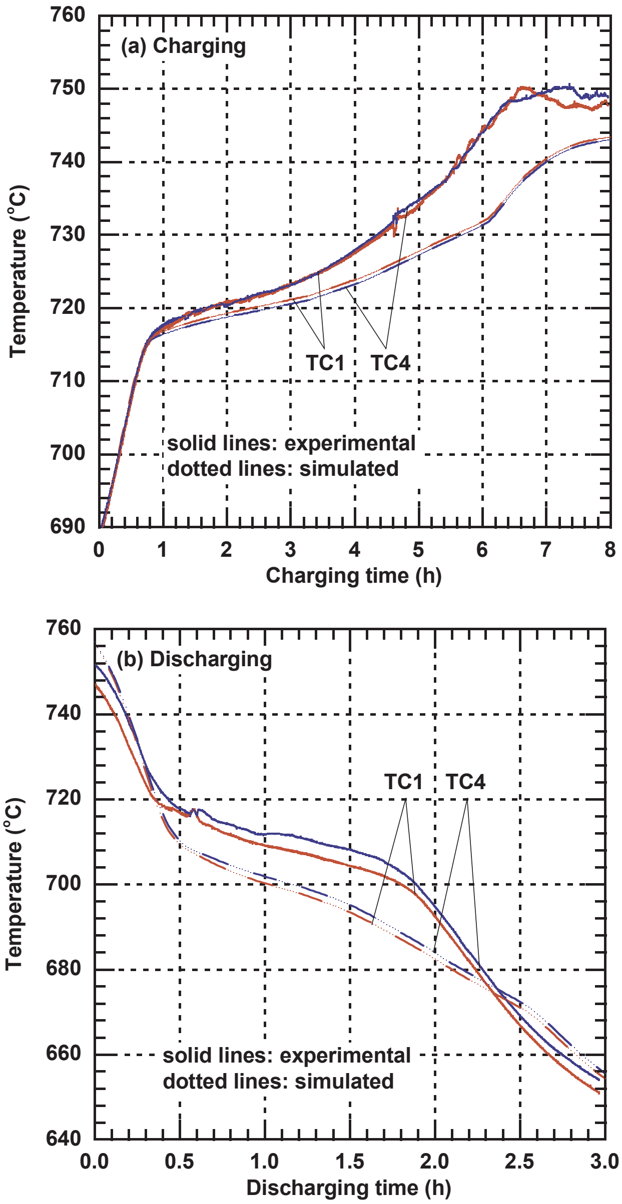

Fig. 13. Temperature comparison of experimental data and simulation results for Prototype 3 during (a) charging and (b) discharging.

Table 3
Comparison for Prototype 1 during charging processes.

	Test 1			Test 2		Test 3	
	TC1	TC2	TC3	TC1	TC2	TC1	TC2
Maximum temperature difference ΔT_{max} (°C)	7.0	4.0	5.0	6.5	12.0	8.0	6.0
Percentage ΔT_{max} based on the melting point of $MgCl_2$ (%)	1.0	0.6	0.7	0.9	1.7	1.1	0.8
Time difference at 730 °C Δt_{730} (h)	−0.5	0.1	−0.1	0.2	0.6	−0.5	0.3
Percentage Δt_{730} based on the total charging time (%)	7.1	1.4	1.4	2.9	8.6	6.2	3.8

Prototype 3 used the same type of GF as Prototype 1. The measurement results were illustrated in Tables 7 and 8. The experimental procedure for Prototype 3 was similar to that for the Prototypes 1 and 2. The comparisons were for the thermocouple locations of TC1, TC4, and TC6 as shown in Fig. 3. The temperature measurements from these

Table 4
Comparison for Prototype 1 during discharging processes.

	Test 1			Test 2		Test 3	
	TC1	TC2	TC3	TC1	TC2	TC1	TC2
Maximum temperature difference ΔT_{max} (°C)	12.0	10.0	9.0	10.0	10.0	10.0	5.0
Percentage ΔT_{max} based on the solidification point of $MgCl_2$ (%)	1.7	1.4	1.3	1.4	1.4	1.4	0.7
Time difference at 700 °C Δt_{700} (h)	−0.5	−0.4	−0.2	−0.4	0.3	−0.5	0.2
Percentage Δt_{700} based on the total discharging time (%)	16.7	13.3	6.7	13.3	10.0	15.3	8.0

Table 5
Comparison for Prototype 2 during charging processes.

	Test 1				Test 2		
	TC1	TC2	TC5	TC6	TC1	TC2	TC5
Maximum temperature difference ΔT_{max} (°C)	4.0	8.0	8.0	11.0	6.0	7.0	10.0
Percentage ΔT_{max} based on the melting point of $MgCl_2$ (%)	0.6	1.1	1.1	1.5	0.8	1.0	1.4
Time difference at 730 °C Δt_{730} (h)	0.4	0.9	0.9	0.6	0.4	0.5	0.8
Percentage Δt_{730} based on the total charging time (%)	5.0	11.2	11.2	7.5	5.0	6.2	10.0

Table 6
Comparison for Prototype 2 during discharging processes.

	Test 1				Test 2		
	TC1	TC2	TC5	TC6	TC1	TC2	TC5
Maximum temperature difference ΔT_{max} (°C)	17.0	12.0	8.0	15.0	17.0	15.0	10.0
Percentage ΔT_{max} based on the solidification point of $MgCl_2$ (%)	2.4	1.7	1.1	2.1	2.4	2.1	1.4
Time difference at 700 °C Δt_{700} (h)	1.0	0.3	0.0	0.4	1.0	0.3	0.1
Percentage Δt_{700} based on the total discharging time (%)	33.3	10.0	0.0	13.3	33.3	10.0	3.3

three thermocouples matched the simulation results with the differences less than 4%.

In addition, Fig. 14 compared the volumetric thermal energy storage of the Prototype 1 as a function of time during charging and discharging experiments. The initial temperatures of the charging process and the discharging process were used as the reference values for the thermal energy storage calculations. The storage medium was absorbing heat from the HTF during the charging process and releasing the stored thermal energy to the HTF during the discharging process. As illustrated in Fig. 14, the experimental data and the simulation results were generally in good agreement. The main reason for the differences between the experimental data and the simulation results during the phase-change processes is because estimation of the latent heat of fusion is sensitive to the temperature, and a small temperature difference can cause a significant thermal energy storage difference between the experiment and the simulation. This is confirmed by the good agreement between the experiment and the simulation observed in the post-phase-change regions.

The comparisons between the experimental data and the numerical simulation results for different types of GFs (Prototype 1, Prototype 2, and Prototype 3) verifies the phase-change simulation model and the thermal properties of the $MgCl_2$/GF composite. The simulation results matched the experimental data quite well for both types of GFs with temperature differences less than 4%. In addition, most of the time differences, at a certain temperature, were less than 15%. Therefore, the thermal properties of the $MgCl_2$/GF composite and the phase-change simulation model can now be applied with confidence to the prediction of the full-scale LHTES system performance and to the design and optimization of large-scale thermal energy storage systems in CSP plants.

5. Conclusions

In this study, a series of tests was conducted on high-temperature laboratory-scale thermal energy storage prototypes with an $MgCl_2$/GF composite as the thermal energy storage medium. The temperature profiles for the charging processes and the discharging processes were generated and compared with the results from numerical simulations using COMSOL Multiphysics commercial software. The following conclusions can be drawn from the experimental data and analyses. First, while the heat transfer characteristics of the $MgCl_2$/GF composite are significantly improved by the addition of the GF, its thermal energy changes during sensible heat-latent heat-sensible heat energy storage and release for the charging and discharging processes follow the typical behavior of the $MgCl_2$ PCM. Second, the temperature profiles as function of time at various locations within each prototype for repeated charging/discharging processes are quite similar, and are within ± 3% of their average value, indicating minimal changes within the storage system. Third, prototypes with GFs of different porosities do not show any significant differences in their thermal performance during charging/discharging processes, which is the consequence of the high GF thermal conductivity as the dominant effect. Fourth, the numerical simulation results match experimental data well for all the prototypes with temperature differences of less than 4% and most of the time differences, at a certain temperature, of less than 15%. These results verify the thermal properties of the $MgCl_2$/GF composite, the phase-change simulation model, and their viable use for the prediction of full-scale LHTES system performance for CSP plants.

Acknowledgements

This work was sponsored by the Solar Energy Technologies Program (SunShot Initiative) of the U.S. Department of Energy under contract number DE-AC02-06CH11357 at Argonne National Laboratory, managed by UChicago Argonne LLC. Discussions with Dr. Levi Irwin and Dr. Avi Schultz (SunShot Initiative) on various aspects of this work are

Table 7
Comparison for Prototype 3 during charging processes.

	Test 1		Test 2			Test 3		
	TC 1	TC 4	TC 1	TC 4	TC 6	TC 1	TC 4	TC 6
Maximum temperature difference ΔT_{max} (°C)	12.0	12.0	9.0	10.0	27.0	6.0	6.0	26.0
Percentage ΔT_{max} based on the melting point of $MgCl_2$ (%)	1.7	1.7	1.3	1.4	3.8	0.8	0.8	3.6
Time difference at 730 °C Δt_{730} (h)	−1.2	−1.2	−0.6	−0.8	−1.4	−0.7	−0.4	−1.4
Percentage Δt_{730} based on the total charging time (%)	−15.0	−15.0	−7.5	−10.0	−17.5	−8.8	−5.0	−17.5

Table 8
Comparison for Prototype 3 during discharging processes.

	Test 1			Test 2			Test 3		
	TC 1	TC 4	TC 6	TC 1	TC 4	TC 6	TC 1	TC 4	TC 6
Maximum temperature difference ΔT_{max} (°C)	12.0	15.0	20.0	17.0	20.0	15.0	20.0	23.0	20.0
Percentage ΔT_{max} based on the solidification point of $MgCl_2$ (%)	1.7	2.1	2.8	2.4	2.8	2.1	2.8	3.3	2.8
Time difference at 700 °C Δt_{700} (h)	0.8	0.7	−0.3	1.0	0.9	−0.15	1.05	0.95	0.0
Percentage Δt_{700} based on the total discharging time (%)	26.7	23.3	−10.0	33.3	30.0	−5.0	35.0	31.7	0.0

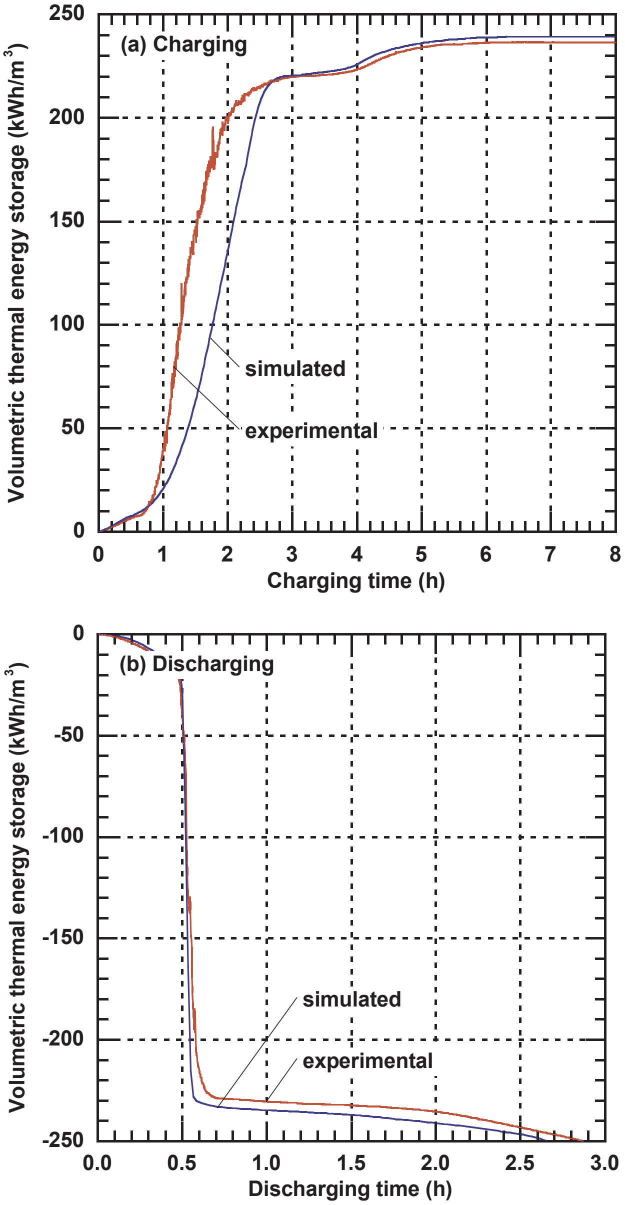

Fig. 14. Thermal energy storage comparison of experimental data and simulation results for Prototype 1 during (a) charging and (b) discharging.

much appreciated. Authors are grateful to Drs. A. Gyekenyesi and M. Singh of Ohio Aerospace Institute for supplying the GrafTech foam billets.

References

Burgaleta, J.I., Arias, S., Ramirez, D., 2011. Gemasolar, the first tower thermosolar commercial plant with molten salt storage. SolarPACES, Granada, Spain, 2011, pp. 20–23.

Faghri, A., Zhang, Y., Howell, J., 2010. Advanced Heat and Mass Transfer. Global Digital Press, Columbia, Missouri.

Guo, C.X., Ma, X.L., Yang, L., 2015. PCM/graphite foam composite for thermal energy storage device. Mater. Sci. Eng. 87, 012014.

Hong, S.T., Herling, D.R., 2006. Open-cell aluminum foams filled with phase change materials as compact heat sinks. Scripta Mater. 55, 887–890.

Janz, G.J., Allen, C.B., Bansal, N.P., Murphy, R.M., Tomkins, R.P.T., 1979. Physical Properties Data Compilations Relevant to Energy Storage. II. Molten Salts: Data on Single and Multi-Component Salt Systems. U.S. Department of Commerce, National Bureau of Standards, Washington, D.C.

Jegadheeswaran, S., Pohekar, S.D., Kousksou, T., 2010. Exergy based performance evaluation of latent heat thermal storage system: a review. Renew. Sustain. Energy Rev. 14, 2580–2595.

Kim, T., France, D.M., Yu, W., Zhao, W., Singh, D., 2014. Heat transfer analysis of a latent heat thermal energy storage system using graphite foam for concentrated solar power. Sol. Energy 103, 438–447.

Krishnan, S., Murthy, J.Y., Garimella, S.V., 2005. A two-temperature model for solid-liquid phase change in metal foams. ASME Trans. J. Heat Transf. 127, 995–1004.

Kuravi, S., Trahan, J., Goswami, D.Y., Rahman, M.M., Stefanakos, E.K., 2013. Thermal energy storage technologies and systems for concentrating solar power plants. Prog. Energy Combust. Sci. 39, 285–319.

Lacroix, M., 1993. Study of the heat transfer behavior of a latent heat thermal energy storage unit with a finned tube. Int. J. Heat Mass Transf. 36, 2083–2092.

Medrano, M., Gil, A., Martorell, I., Potau, X., Cabeza, L.F., 2010. State of the art on high-temperature thermal energy storage for power generation. Part 2-Case studies. Renew. Sustain. Energy Rev. 14, 56–72.

Miliozzi, A., Liberatore, R., Crescenzi, T., Veca, E., 2015. Experimental analysis of heat transfer in passive latent heat thermal energy storage systems for CSP plants. Energy Proc. 82, 730–736.

Nithyanandam, K., Pitchumani, R., 2013. Design and analysis of metal foam enhanced latent thermal energy storage with embedded heat pipes for concentrating solar power plants. In: Proceedings of ASME 2013 7th International Conference on Energy Sustainability and 11th Fuel Cell Science.

Ohsenbrügge, C., Marth, W., yde Sosa, I.N., Drossel, W.G., Voigt, A., 2016. Reduced material model for closed cell metal foam infiltrated with phase change material based on high resolution numerical studies. Appl. Therm. Eng. 94, 505–512.

Poling, B.E., Thomson, G.H., Friend, D.G., Rowley, R.L., Wilding, W.V., 2008. Perry's Chemical Engineers' Handbook, eighth ed. McGraw-Hill, New York.

Robak, C.W., Bergman, T.L., Faghri, A., 2011. Enhancement of latent heat energy storage using embedded heat pipes. Int. J. Heat Mass Transf. 54, 3476–3484.

Samara, F., Groulx, D., Biwole, P.H., 2012. Natural convection driven melting of phase change material: comparison of two methods. In: Proceedings of the 2012 COMSOL Conference in Boston.

Shabgard, H., Bergman, T.L., Sharifi, N., Faghri, A., 2010. High temperature latent heat thermal energy storage using heat pipes. Int. J. Heat Mass Transf. 53, 2979–2988.

Siahpush, A., O'Brien, J., Crepeau, J., 2008. Phase change heat transfer enhancement using copper porous foam. ASME Trans. J. Heat Transf. 130, Paper number 082301.

Siegel, R., 1977. Solidification of low conductivity material containing dispersed high conductivity particles. Int. J. Heat Mass Transf. 20, 1087–1089.

Singh, D., Kim, T., Zhao, W., Yu, W., France, D.M., 2016. Development of graphite foam infiltrated with $MgCl_2$ for a latent heat based thermal energy storage (LHTES) system. Renewable Energy 94, 660–667.

Singh, D., Zhao, W., Yu, W., France, D.M., Kim, T., 2015. Analysis of a graphite foam-NaCl latent heat storage system for supercritical CO_2 power cycles for concentrated solar power. Sol. Energy 118, 232–242.

Velraj, R., Seeniraj, R.V., Hafner, B., Faber, C., Schwarzer, K., 1997. Experimental analysis and numerical modelling of inward solidification on a finned vertical tube for a latent heat storage unit. Sol. Energy 60, 281–290.

Wu, B., Xing, Y., 2010. Numerical study of graphite foams saturated with phase change materials in power system thermal management. IEEE, 978-1-4244-4813-5/10.

Zalba, B., Marin, J.M., Cabeza, L.F., Mehling, H., 2003. Review on thermal energy storage with phase change: materials, heat transfer analysis and applications. Appl. Therm. Eng. 23, 251–283.

Zhao, C.Y., Wu, Z.G., 2011. Heat transfer enhancement of high temperature thermal energy storage using metal foams and expanded graphite. Sol. Energy Mater. Sol. Cells 95, 636–643.

Zhao, W., France, D.M., Yu, W., Kim, T., Singh, D., 2014. Phase change material with graphite foam for applications in high-temperature latent heat storage systems of concentrated solar power plants. Renewable Energy 69, 134–146.